JACS
JOURNAL OF THE AMERICAN CHEMICAL SOCIETY

ARTICLE

pubs.acs.org/JACS

Probing Dynamic Generation of Hot-Spots in Self-Assembled Chains of Gold Nanorods by Surface-Enhanced Raman Scattering

Anna Lee,[†] Gustavo F. S. Andrade,[‡] Aftab Ahmed,[§] Michele L. Souza,[‡] Neil Coombs,[†] Ethan Tumarkin,[†] Kun Liu,[†] Reuven Gordon,[*,§] Alexandre G. Brolo,[*,‡] and Eugenia Kumacheva[*,†]

[†]Department of Chemistry, University of Toronto, 80 Saint George Street, Toronto, Ontario M5S 3H6, Canada

[‡]Department of Chemistry, University of Victoria, P.O. Box 3065, Victoria, British Columbia V8W 3V6, Canada

[§]Department of Electrical and Computer Engineering, University of Victoria, Victoria, British Columbia V8W 3P6, Canada

Supporting Information

ABSTRACT:

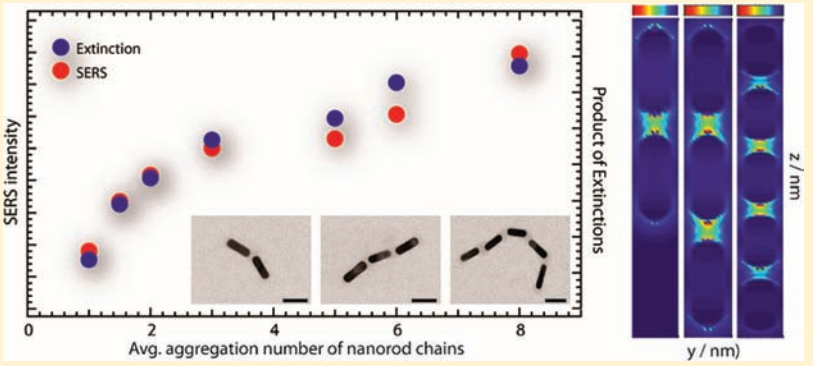

Further progress in the applications of self-assembled nanostructures critically depends on developing a fundamental understanding of the relation between the properties of nanoparticle ensembles and their time-dependent structural characteristics. Following dynamic generation of hot-spots in the self-assembled chains of gold nanorods, we established a direct correlation between ensemble-averaged surface-enhanced Raman scattering and extinction properties of the chains. Experimental results were supported with comprehensive finite-difference time-domain simulations. The established relationship between the structure of nanorod ensembles and their optical properties provides the basis for creating dynamic, solution-based, plasmonic platforms that can be utilized in applications ranging from sensing to nanoelectronics.

INTRODUCTION

Organization of individual nanoparticles (NPs) into hierarchical nanostructures — superlattices or small clusters — constitutes a frontier area of research in nanoscience. While NPs alone offer many scientific challenges and applications, ensembles of NPs show unique coupled properties that potentially can be exploited in functional nanoscale devices.[1−6]

Self-assembly of NPs offers a simple, cost-efficient, solution-based method for producing ensembles of NPs, as well as the ability to fabricate nanostructures on nonplanar substrates.[7−12] Currently, self-assembled nanostructures composed of metal, semiconductor, and magnetic NPs have shown applications in the areas of data storage, imaging, and sensing of chemical and biochemical species.[13−21] The utilization of self-assembled nanostructures in other applications, in comparison with those produced by nanofabrication techniques, is limited by the difficulty in generating defect-free structures with precisely controlled geometry and distance between the NPs. Further more, fundamental understanding has to be developed on the relationship between the properties of self-assembled NP clusters and their dynamic structural characteristics such as aggregation number, mutual NP orientation, and interparticle distance. With this framework in place, it would be possible to predict the properties of self-assembled structures, both theoretically and practically, in a reproducible fashion.

In the particular case of metal nanocrystals, gold NPs with various shapes have been organized in a broad range of nanostructures including chains, two-dimensional sheets, and superlattices.[22−26] In comparison with isotropic, shape-symmetric NPs, the self-assembly of gold nanorods (NRs) leads to more interesting, and potentially more useful applications, as it provides the ability to exploit vectorial properties of the resulting nanostructures.[27−29] Typically, optical properties of ensembles of gold NRs are characterized by measurements of extinction in the visible and near-infrared (NIR) spectral ranges. Individual

Received: February 17, 2011
Published: April 22, 2011

gold NRs show two types of localized surface plasmon resonances (LSPRs), due to the coherent oscillations of the conduction band electrons in directions that are parallel and perpendicular to the long NR axis.[30,31] End-to-end assembly of gold NRs in chains leads to the coupling of alternating dipoles along the chain, which results in a red shift of the longitudinal LSPR. Side-by-side assembly of NRs results in a blue shift of longitudinal LSPR and a red shift of the transverse LSPR.[30,32,33]

Coupling of LSPRs in chains of gold NRs results in the formation of a periodic array of enhanced electric fields (hot-spots) in the spaces between the NR ends. Thus, self-organization of gold NRs offers a tool for studies of optical properties of ordered NR ensembles by surface-enhanced Raman scattering (SERS). Furthermore, the dynamic self-assembly of NRs in well-defined, one-dimensional nanostructures provides the ability to explore the role of order in NR ensembles on their SERS properties. Currently, the majority of studies of hot-spots have been carried out for NP assemblies with a limited degree of order,[34−36] which led to the insufficient understanding of the effect of structural characteristics of the aggregates on their SERS properties. In addition, research has been focused on isolated NP aggregates ("single particle" SERS), and an understanding of the properties of the system comprised of many NP assemblies remains elusive. In an attempt to achieve greater control over hot-spot generation in NP clusters, recent studies have focused on SERS of self-assembled dimers and trimers of spherical gold NPs in single-aggregate and ensemble-averaged systems.[37−39] However, currently, only a single report exists on the generation of hot-spots in self-assembled chains of gold NRs. This report is focused on the reorientation of analyte molecules in the gaps between NR ends.[40]

Here we report the results of experimental and theoretical studies of the relationship between the dynamic structural characteristics of self-assembled clusters of gold NRs and their ensemble-averaged SERS properties resulting from the controlled generation of plasmonic electromagnetic hot-spots. We took advantage of the geometrical and chemical anisotropy of NRs to induce their assembly in chains in an end-to-end fashion. In the course of assembly, the dielectric environment and the spacing between adjacent NRs remained constant. The process was monitored by correlating the average aggregation number of NRs in the chains with their extinction and ensemble-averaged SERS signals (presently, such a correlation has been demonstrated only for nanostructures fabricated by the top-down method).[41,42] The experimental findings were supported by the results of finite-difference time-domain simulations of the optical properties of NR assemblies. Our work establishes a strong link between experiment and theory, and it provides an important insight into the properties of hot-spots in ordered, solution-based nanostructures. In addition to the fundamental importance of these results, the established relationship between the structure of NR assemblies and their optical properties provides the basis for the development of new design rules for the generation of nanostructures with applications spanning from biomedicine to nanoelectronics.

EXPERIMENTAL SECTION

Synthesis of Gold NRs. Gold NRs were prepared by the "seed-mediated growth method" devised by El-Sayed et al.[43] Briefly, seed NPs were obtained by the reduction of $HAuCl_4$, dissolved in an aqueous solution of cetyltrimethylammonium bromide (CTAB), with cold sodium borohydride ($NaBH_4$). The growth solution was prepared by dropwise addition of ascorbic acid in an aqueous solution of $HAuCl_4$, CTAB, and $AgNO_3$. A seed solution aged for 5 min was added to the growth solution, and the NR growth was initiated. The color of the solution mixture changed from clear to deep purple after incubation for 10 h at 27 °C. The resultant CTAB-coated gold NRs were purified by two centrifugation cycles (8500 rpm for 30 min). In the next step, we conducted exchange of CTAB ligands attached to the ends of NRs with thiol-terminated polystyrene (SH-PS, Polymer Source Inc.) with a molecular weight of 12 000 g/mol[28] and polydispersity index of 1.09. Approximately 0.5 mL of the concentrated aqueous solution of CTAB-coated NRs (∼1.0 mg/mL) was rapidly injected under sonication into 10 g of THF solution containing 5 mg of SH-PS (∼0.05 wt %). The mixture was sonicated for 30 min at 42 kHz (±0.6%) and incubated at room temperature for 24 h. The resultant NRs were further purified by seven centrifugation cycles at 8500 rpm for 30 min. A concentrated solution of PS-functionalized NRs was collected and redispersed in THF to form a stock solution.

End-to-End Self-Assembly of NRs. Prior to the self-assembly experiments, 760 μL of tetrahydrofuran (THF) was evaporated from the stock NR solution. The dried NRs were redissolved in 2.45 mL of dimethylformamide (DMF). A solution of the Raman reporter molecule Oxazine 720 (OX) in DMF (4 μM) was added dropwise under shaking to the NR solution in DMF. Following 30 min of agitation under gentle vortex conditions, the mixture was incubated for 1 h. End-to-end self-assembly of the NRs was triggered by dropwise addition of the DMF/water mixture, containing 20 vol % of water. As soon as NR self-assembly began we carried out, at regular time intervals, parallel extinction and SERS measurements, as well as the preparation of samples for electron microscopy experiments.

Characterization of Self-Assembled NR Structures. Scanning transmission electron microscopy (STEM) images of individual NRs and self-assembled NR chains were obtained using a Hitachi S-5200 field emission SEM equipped with a transmitted electron detector operating at 30 kV. Extinction measurements were carried out using a Varian Cary 5000 UV−visible−NIR spectrometer.

In SERS measurements, 1.5 mL of the solution of self-assembled NRs was placed in a vial. Raman spectra excited with a 785 nm laser line were acquired with a Renishaw InVia System spectrometer coupled to a Leica microscope. The laser power was set to 1% of the full power (approximately 80 μW). The laser beam was focused on the sample by a 5× objective lens (NA = 0.12). The calculated interrogated volume was 6.46 nL. The spectra were measured with a 4 cm^{-1} resolution, using a 1 s exposure and 25 scans.

Control SERS experiments were conducted using a roughened gold substrate. A solid gold electrode with surface area of 0.3 cm^2 was roughened with 20 successive oxidation−reduction cycles from −0.3 to +1.25 V at 100 mV/s in an aqueous 0.1 M KCl working solution. The electrode was then isolated from the electrochemical cell and exposed to a 4 μM solution of OX in water, in pure DMF, or in the DMF/water mixture (20 vol % of water). After 15 min exposure, the surface was rinsed with an appropriate solvent, that is, with water, DMF, or the DMF/water mixture, and dried under nitrogen flux. The SERS spectra of OX adsorbed to the gold substrate were acquired using excitation at 785 nm (laser power 1%, four accumulations, and 5 s exposure time).

Simulations. The assembly of NR chains was simulated by the finite difference time domain (FDTD) method.[44] Polarization of the incident field was parallel to the long NR axis. The simulation domain was terminated with perfectly matched layer (PML). The complex permittivity of gold was modeled using the experimental data of Johnson and Christy.[45] To calculate the absorption and scattering cross sections of NR chains, we employed the formalism of the total field scattered field (TFSF). We introduced a set of two-dimensional power monitors, which formed two surfaces enclosing the NRs, one inside the TF region

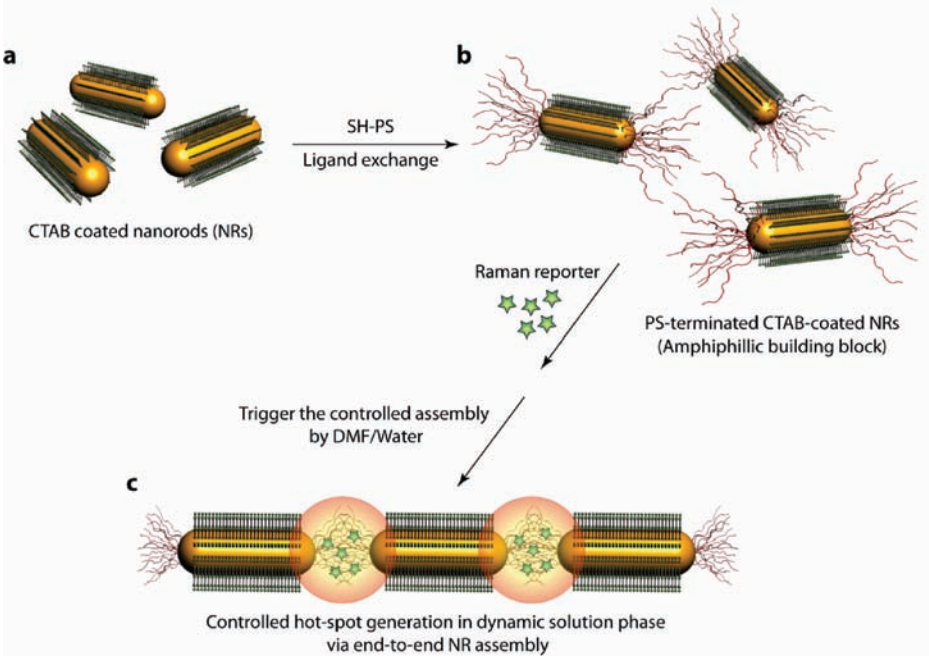

Figure 1. Schematic of the generation of hot-spots via end-to-end self-assembly of gold NRs in chains. (a) Gold NRs stabilized with CTAB. (b) Ligand exchange of CTAB with SH-PS at the edges of the NRs. (c) End-to-end assembly of NRs triggered by adding water to the solution of NRs in DMF, in the presence of Raman reporter OX. The volume fraction of water in the DMF/water mixture is 20 vol %. Hot-spots are generated between the ends of adjacent NRs. The distance between the adjacent NRs in the chain is maintained constant. Schematic is not drawn to scale.

(power monitor 1, or PM1) and the other one in the SF region (power monitor 2, or PM2). We calculated the absorption cross section of the nanostructures by evaluating the net power flow into PM1, which represented the power loss in the NRs. The total power exiting PM2 was used for the calculation of the scattering cross section as $\sigma_{scat} = P_{scat}/I_s$, where P_{scat} is the scattered power obtained from PM2 and I_s is the intensity of the light source. The extinction cross section was determined by the summation of scattering and absorption cross sections.

RESULTS AND DISCUSSION

Figure 1 illustrates site-specific functionalization of gold NRs and dynamic generation of hot-spots via end-to-end NR assembly. The NRs with a mean length of 37.6 ± 4.4 nm and a mean diameter of 11.4 ± 1.0 nm were used as the building blocks of the chains. In the ligand-exchange step, SH-PS replaced CTAB at the ends of NRs, transforming them into amphiphilic species.[28] These NRs were well-dispersed in DMF, a good solvent for both the CTAB molecules coating the long sides of the NRs and the SH-PS molecules attached to the NR ends.[28] End-to-end assembly of the NRs was triggered by introducing 20 vol % of water to the solution of amphiphilic NRs in DMF in the presence of the Raman reporter, OX. With the addition of water, the mixture became a poor solvent for the PS ligands localized at NR ends but remained a good solvent for the hydrophilic CTAB ligands coating the long side of the NRs. In order to avoid unfavorable contact of PS molecules with the DMF/water solution and to reduce the surface energy of the system, the NRs associated in the end-to-end manner.

Figure 2a shows representative STEM images of the NR assemblies in various stages of chain growth. STEM imaging was carried out at low voltage (30 kV), which is suitable for imaging organic macromolecules. All the images were acquired without staining. The diffuse gray regions between the ends of adjacent NRs in the chains correspond to the globules of SH-PS molecules that formed in the poor DMF/water solvent. Using image analysis, we determined that the average distance between the ends of adjacent NRs throughout the self-assembly process remained 8.9 ± 1.5 nm. We note that, while STEM images are valuable in determining the average aggregation number of NRs in the chain and inter-NR spacing, the conformation of the chain may be influenced by the drying process. Therefore, the precise conformation of the chains in solution cannot be directly inferred from the micrographs presented in Figure 2a.

The evolution of NR chains in the course of self-assembly was characterized by the change in their average aggregation number $\bar{X}_n$ as

$$\bar{X}_n = \frac{N_0}{N_{tot}} = \frac{\sum n_x x}{\sum n_x} \quad (1)$$

where N_0 and N_{tot} are the number of NR chains and the total number of NRs in the system, respectively, and n_x is the number of chains containing x NRs, respectively. The values of $\bar{X}_n$ were calculated by analyzing STEM images of the nanochains formed in the course of self-assembly experiments. The kinetics of growth of the NR chains resembled the evolution of polymer chains in reaction-controlled step-growth polymerization, as reported in our earlier work;[46] however, the self-assembly of the NRs in the presence of OX occurred at a greatly increased rate in comparison with the OX-free system.

The extinction and SERS measurements were carried out within the time of self-assembly t from ~5 min to 18 h, concurrent with the collection of samples for STEM imaging. Figure 2b shows the evolution of the extinction spectra of the system undergoing self-assembly. In the course of chain growth,

dx.doi.org/10.1021/ja2015179 |J. Am. Chem. Soc. 2011, 133, 7563–7570

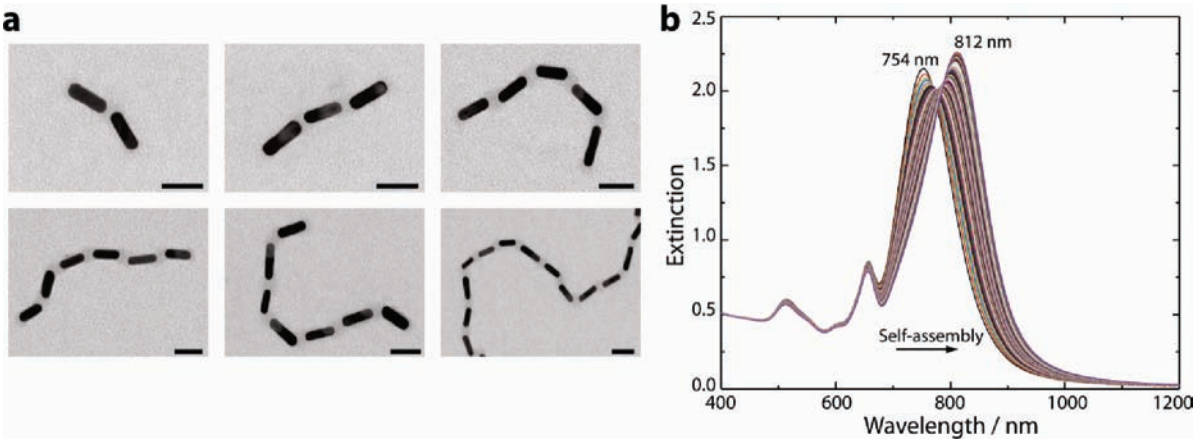

Figure 2. (a) Representative STEM images of the self-assembled chains of NRs. Diffuse gray regions between adjacent NRs indicate the presence of SH-PS globules forming in a poor solvent. Scale bar is 40 nm. (b) Variation in extinction properties of NRs in the course of their self-assembly in chains. The spectral position of LSPR shifts from 754 to 812 nm, with the aggregation number of the NR chains changing from 1 at $t < 5$ min to 8 at $t = 18$ h. Transverse LSPR is located at 514 nm. The peak at 660 nm corresponds to OX.

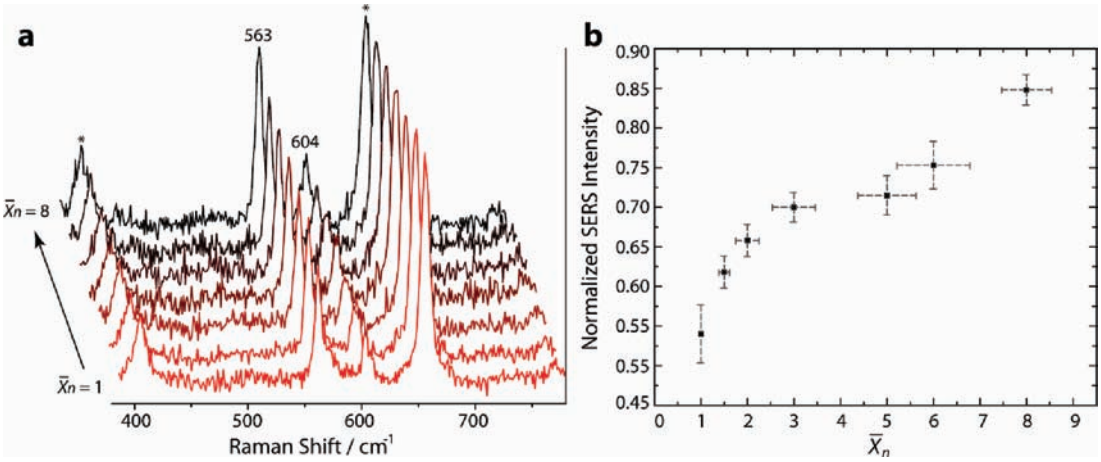

Figure 3. (a) Evolution of normalized ensemble-averaged SERS spectra in self-assembled NR chains. The average aggregation number of NR assemblies changes from $\bar{X}_n = 1$ at $t < 5$ min (bright-red spectrum) to 8 at $t = 18$ h (black spectrum). The SERS peaks at 563 and 604 cm^{-1} are normalized against the SERS peak of DMF at 659 cm^{-1} (indicated with asterisks). (b) Variation in the normalized SERS peak intensity measured at 563 cm^{-1} plotted as a function of the average aggregation number of the NR chains. SERS variation (y error) is based on three measurements taken within 15 min. Approximately 1000 NRs (including individual species) were used in the calculations of number of NRs (x error). Laser excitation wavelength was 785 nm.

the longitudinal LSPR peak shifted from 754 to 812 nm, due to the coupling of alternating dipoles along the NR chain. The end-to-end arrangement led to the reduction in resonance energy with respect to individual NRs.[30,32,33,47−49] In the course of self-assembly, the width of the longitudinal LSPR peak broadened by ∼12% when the aggregation number increased from 1 to 8, which was significantly narrower than for solution-based aggregates of gold NPs reported to date. The absorption peak at 659 nm corresponded to OX molecules. This peak was not noticeably shifted or reduced in intensity for a period of at least 18 h, which suggested good structural and temporal stability of OX during NR self-assembly.

Figure 3a illustrates the evolution of the ensemble-averaged SERS spectra of OX in the course of the self-assembly experiments. The most enhanced bands at 563 and 604 cm^{-1} (assigned to vibrational modes of the phenoxazine ring of the dye)[50,51] were consistent with the Raman spectrum of the solution of OX in DMF (Supporting Information, Figure S1). The same values of vibrational frequencies for OX adsorbed on the surface of NRs and for the solution of OX in DMF suggested that the reported molecule was physisorbed onto the gold surface.[52]

By exploiting the sensitivity of SERS spectra to changes in their local environment, we determined the location of OX with respect to the CTAB-coated long NR sides and SH-PS-capped NR edges. In principle, OX could be localized within the CTAB layer and/or could be associated with SH-PS molecules at the NR ends. In the first instance, the localization of OX could be dominated by the hydrophobic interactions with hydrocarbon chains of CTAB, since the localization of positively charged OX molecules in the vicinity of the cationic groups of CTAB was less likely. Alternatively, OX could be associated with the SH-PS ligands, so that the nonpolar component of the dye would interact with hydrophobic PS molecules, and its polar head would be in the solvent environment.

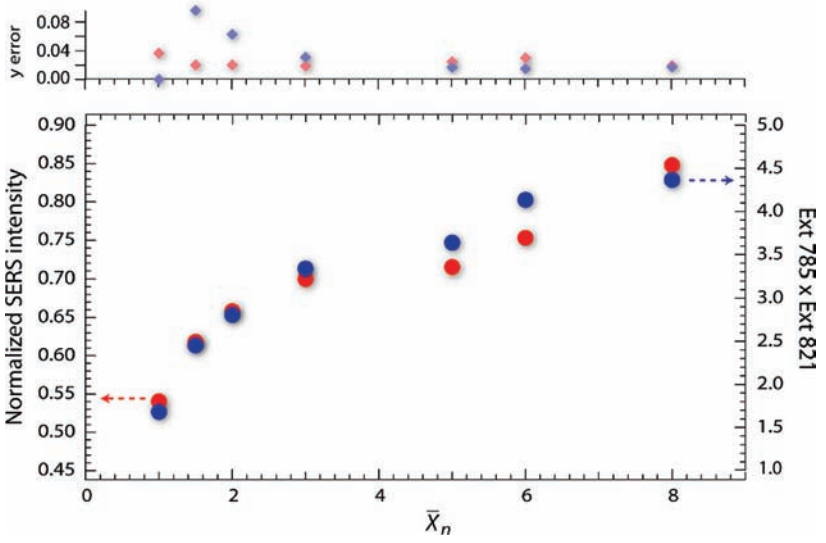

Figure 4. Correlation of the normalized intensity of SERS peak at 563 cm^{-1} (red circles) and the product of extinctions measured at 785 and 821 nm (blue circles), plotted as a function of the average aggregation number $\bar{X}_n$ of the NR chains. Top: *y* errors of the intensity of SERS peak (red squares) and the product of extinctions (blue squares) were calculated on the basis of three measurements.

To address the question of the predominant localization of the dye in the NR chains, we carried out a series of control SERS experiments with OX dissolved in several solvents, namely, water, DMF, and the DMF/water mixture at a water content of 20 vol %. The experiments were conducted using a roughened gold substrate. The SERS frequency of the strongest OX band in the 500−600 cm^{-1} region depended on the type of solvent: In water, the SERS band was centered at 595 cm^{-1}, similar to previously reported results.[50,51] In DMF, the spectral position of the peak was 567 cm^{-1} (Supporting Information, Figure S2). In the DMF/water mixture, the SERS spectrum of OX featured two peaks located at 595 and 567 cm^{-1} (Figure S2).

For the self-assembled NR chains, the main SERS peak of OX was measured at 563 cm^{-1}, very close to 567 cm^{-1}, suggesting that OX was located in a DMF environment. The absence of a shoulder at 595 cm^{-1} (Figure S2) suggested that no appreciable interactions existed between OX and water. Therefore, it was reasonable to conjecture that OX was predominately localized within the hot-spot region between the ends of the NRs from which water is largely excluded. We note that this did not rule out the possibility of OX molecules being located in the hydrophobic environment in the CTAB layer; however, the species outside the hot-spots did not significantly contribute to the overall SERS signal. Furthermore, the fact that the vibrational frequency of OX at 563 cm^{-1} did not change in the course of assembly indicated that the location of physisorbed OX remained unaltered. The relative intensities of the bands of OX at 563 and 604 cm^{-1} also remained constant throughout the process of self-assembly, suggesting that OX retained its orientation and geometry with respect to the NR surface without any appreciable molecular reorientation.[53,54]

The change in the SERS intensity was determined over the course of NR self-assembly by using the intensity of the peak corresponding to DMF vibration at 659 cm^{-1} as an internal standard. Figure 3b shows the variation in the ratio of intensities of the peak at 563 cm^{-1} of OX to the intensity of the peak at 659 cm^{-1}, plotted as a function of $\bar{X}_n$. Importantly, the change in ensemble-averaged normalized SERS intensity was not monotonic: it increased for $1 \leq \bar{X}_n \leq 3$, leveled off for $3 \leq \bar{X}_n \leq 5$, and increased again for $5 \leq \bar{X}_n \leq 8$.

To understand this nonlinear behavior, we considered only SERS arising from the electromagnetic effect. Under resonance conditions, the incident light absorbed by the nanostructure generates localized surface plasmons, thereby creating a strong local electromagnetic field, $E_{loc}(\omega_{exc})$, close to the surface of the NRs. This effect leads to the enhancement in intensity of the Raman scattered light by the OX molecule, which is assumed to be a point dipole. The scattered light also excites localized surface plasmons and generates an enhanced field, $E_{loc}(\omega_{RS})$, at the Raman Stokes frequency. The field enhancement G_{SERS} is proportional to the square of the product of the local field at the incident frequency and the local field at the scattered Raman Stokes frequency,[42,55−58] that is,

$$G_{SERS} \propto |E_{loc}(\omega_{exc})E_{loc}(\omega_{RS})|^2 \qquad (2)$$

As discussed above, light extinction (absorption + scattering) at wavelengths matching the resonances of the nanostructure generates LSPR that leads to field localization. Therefore, a correlation between the SERS efficiency and the product of extinctions at ω_{exc} and ω_{RS} should be expected.

We plotted the variations in the normalized SERS intensity and the product of the extinctions measured at the excitation wavelength of 785 nm (ω_{exc}) and at the wavelength of the Stokes-shifted radiation of 821 nm (ω_{RS}) versus the average aggregation number, $\bar{X}_n$, of the NR chains (Figure 4). In the course of NR self-assembly, the product of extinctions varied, since the spectral position of the longitudinal LSPR gradually red-shifted (see Figure 2). Figure 4 shows a strong correlation between the variation in SERS intensity and the product of extinctions, both plotted as a function of $\bar{X}_n$. Such correlation indicated that the variation in SERS properties with NR assembly indeed originated from the inherent electromagnetic properties of the self-assembled nanostructure, rather than from chemical effects. In addition, the results shown in Figure 4 suggested a narrow distribution of hot-spots, confirming the high level of

dx.doi.org/10.1021/ja2015179 |*J. Am. Chem. Soc.* 2011, 133, 7563–7570

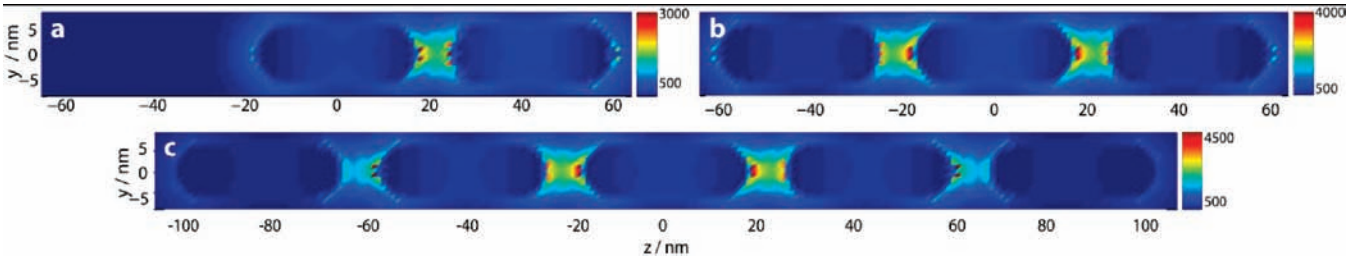

Figure 5. Three-dimensional finite-difference time-domain (3D-FDTD) simulation of the end-to-end assembly of gold NRs. Electric field profile was calculated at the resonance wavelength of the collinear NR chain at (a) 760, (b) 782, and (c) 802 nm. Polarization of the incident light is parallel to the long axes of the NRs (i.e., to the *z*-coordinate). Hot-spots between adjacent NRs show a maximum electric field intensity 4000 times greater than the incident field.

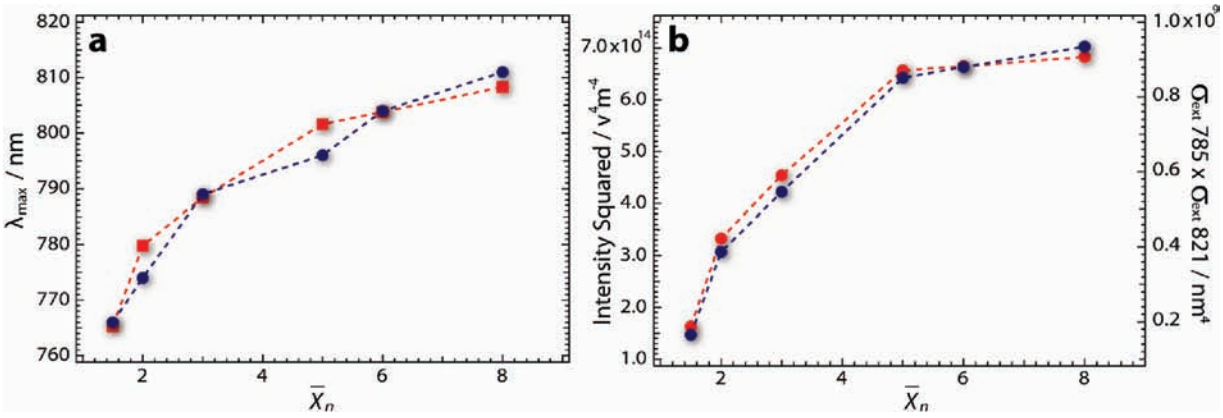

Figure 6. (a) Variation in experimentally measured (blue circles) and calculated (red squares) spectral position of the longitudinal LSPR, plotted as a function of the average aggregation number, $\bar{X}_n$, of the NR chains. (b) Variation in the calculated product of the squares of the electric field (intensity) at 785 and 821 nm (red circles) and the product of the extinction cross sections at 785 and 821 nm (blue circles), plotted vs $\bar{X}_n$.

organization of the dynamic self-assembled system in solution. We note that a direct correlation between extinction and SERS is qualitatively followed in simple nanostructures such as individual gold spheres[59] and organized arrays, but it falls apart dramatically in strongly coupled random systems with a large distribution of spatially localized resonances.[60]

In order to further highlight the relationship between SERS enhancement and the dynamic evolution of hot-spots, we conducted comprehensive FDTD simulations by numerically solving Maxwell's curl equations by iteration over time.[44] Figure 5 shows examples of electric field (E field) profiles corresponding to different wavelengths for the chains of collinearly assembled NRs. The field inside individual NRs rapidly decayed, while hot-spots between adjacent NRs exhibited a maximum E field intensity 4000-fold greater than the intensity of the incident field.

In our work, the self-assembled NR chains were characterized by the distribution of their aggregation numbers and the variation in the angle between adjacent NRs within the chain. In order to examine the role of the distribution in $\bar{X}_n$ of the NR chains, we performed FDTD simulations for chains with different lengths and then used experimentally determined aggregation statistics to calculate the electric field intensities (Supporting Information, Figure S3). For $\bar{X}_n$ = 8, the E field intensity squared had the largest value when normalized with respect to the aggregation number of the chain (Figure S3a), which was consistent with experimental results shown in Figure 3. While the longer chains had a lower maximum intensity, they also had a weaker variation in their maximum intensity wavelength compared to the shorter chains (Figure S3b). This spectral purity provided greater enhancement in the E field when statistically averaged.

When the distribution in the aggregation numbers was not taken into account, the field intensity was highest for chains containing three NRs, when normalized by the number of NRs in the chain (Figure S3b). This effect originated from the trade-off between the local field enhancement and optical absorption (that is, loss) in the NR chains. A figure of merit that compares the local field enhancement to the loss is the ratio between the real and imaginary parts of the relative permittivity of the NRs. For gold, this figure of merit is at a maximum at ~760 nm, close to the resonance wavelength of the trimer structure.

Since the SERS and LSPR properties of the NR assemblies depend on the collinearity of the NRs with respect to the long axis of the chain,[32,33,48] we have performed FDTD calculations for dimers and trimers of NRs with varying orientations with respect to each other (Supporting Information, Figure S4). The deviation from collinearity at the angles between the long axes of the NRs of 20, 40, 60, and 90° resulted in a significant reduction of extinction and, thus, decreasing E field intensity (Figure S4). This result implied that in ensemble measurements, the greatest contribution to extinction and SERS arose from the chains with a collinear NR arrangement, with a minor influence on E field intensity from "off-axis" NRs.

dx.doi.org/10.1021/ja2015179 |*J. Am. Chem. Soc.* 2011, 133, 7563–7570

The persistence length of the chains formed by the 40-nm-long NRs in the DMF/water mixture with 20 vol % of water was 230 nm, corresponding to $\bar{X}_n \approx 6$.[28a] We admit that chain conformations determined from the TEM images of dried samples or from the AFM images of the chains on the solid substrate under solution may not accurately reflect the configuration of chains in solution. Therefore, extensive cryo-TEM experiments followed by the deliberate analysis of the statistical distribution of angles along the chains with different aggregation numbers will provide more insight into the relationship between the SERS properties and the chain flexibility.

For the calculation of scattering and absorption cross sections, we employed the total field/scattered field method for the separation of the scattered field from the incident radiation. Our calculations showed that the extinction cross-section mainly originated from NR absorption, whereas the contribution from scattering was minor (Supporting Information, Figure S5). Experimental and calculated results obtained for the extinction (Figure S5) and variations in the spectral position of the longitudinal LSPR (Figure 6a) were in good agreement when NR number distribution was considered. Figure 6b shows the change in the calculated extinctions (a product of those measured at 785 and 821 nm) and E field intensity squared as a function of $\bar{X}_n$. A strong correlation between the two trends was consistent with the relationship expressed in eq 2. Significantly, the experimental results (Figure 4) and theoretical results shown in Figure 6b are in good qualitative agreement.

CONCLUSIONS

Following dynamic generation of hot-spots via controlled, solution-based self-assembly of gold NR chains, we have established a direct relationship between extinction and SERS properties of the chains. An important aspect of our experiments included the formation of ensembles with a well-defined, invariant distance between adjacent NRs. Our work opens the way for studies of optical properties of other geometry-dependent dynamic plasmonic systems, e.g., ensembles of side-by-side gold NRs and compartmentalization of molecules or particles in hot-spots. Building from the correlation between SERS and extinction, practical applications of self-assembled structures ranging from chemical and biological sensing to nanoelectronics, e.g., plasmonic circuits, become a step closer.

ASSOCIATED CONTENT

Supporting Information. Figures S1−S5. This material is available free of charge via the Internet at http://pubs.acs.org.

AUTHOR INFORMATION

Corresponding Author

agbrolo@uvic.ca; rgordon@uvic.ca; ekumache@chem.utoronto.ca

ACKNOWLEDGMENT

A.L. and E.K. thank Shun Lo, Christina McLaughlin, James Li, and Prof. Gilbert Walker (University of Toronto). G.F.S.A. and M.L.S. thank the Canadian Bureau for International Education, Department of Foreign Affairs and International Trade (CBIE-DFAIT) for fellowships for postdoctoral research and an Emerging Leaders of Americas Partnership (ELAP) program. All authors thank NSERC Canada for financial support of the Strategic Network for Bioplasmonic Systems (Biopsys) and thank Lumerical, Inc.

REFERENCES

(1) Claridge, S. A.; Castleman, A. W.; Khanna, S. N.; Murray, C. B.; Sen, A.; Weiss, P. S. *ACS Nano* **2009**, *3*, 244–255.
(2) Glotzer, S. C.; Solomon, M. J. *Nat. Mater.* **2007**, *6*, 557–562.
(3) Grzelczak, M.; Vermant, J.; Furst, E. M.; Liz-Marzan, L. M. *ACS Nano* **2010**, *4*, 3591–3605.
(4) Mann, S. *Nat. Mater.* **2009**, *8*, 781–792.
(5) Nie, Z. H.; Petukhova, A.; Kumacheva, E. *Nat. Nanotech.* **2010**, *5*, 15–25.
(6) Srivastava, S.; Kotov, N. A. *Soft Matter* **2009**, *5*, 1146–1156.
(7) Lee, A.; Coombs, N. A.; Gourevich, I.; Kumacheva, E.; Scholes, G. D. *J. Am. Chem. Soc.* **2009**, *131*, 10182–10188.
(8) Tang, Z. Y.; Zhang, Z. L.; Wang, Y.; Glotzer, S. C.; Kotov, N. A. *Science* **2006**, *314*, 274–278.
(9) Shevchenko, E. V.; Talapin, D. V.; Kotov, N. A.; O'Brien, S.; Murray, C. B. *Nature* **2006**, *439*, 55–59.
(10) Zhang, S. Z.; Kou, X. S.; Yang, Z.; Shi, Q. H.; Stucky, G. D.; Sun, L. D.; Wang, J. F.; Yan, C. H. *Chem. Commun.* **2007**, 1816–1818.
(11) Zhuang, J. Q.; Wu, H. M.; Yang, Y. A.; Cao, Y. C. *J. Am. Chem. Soc.* **2007**, *129*, 14166–14167.
(12) Jones, M. R.; Macfarlane, R. J.; Lee, B.; Zhang, J. A.; Young, K. L.; Senesi, A. J.; Mirkin, C. A. *Nat. Mater.* **2010**, *9*, 913–917.
(13) Wang, Z. L. *Adv. Mater.* **2003**, *15*, 432–436.
(14) Tseng, R. J.; Tsai, C. L.; Ma, L. P.; Ouyang, J. Y. *Nat. Nanotech.* **2006**, *1*, 72–77.
(15) Lee, J.; Hernandez, P.; Govorov, A. O.; Kotov, N. A. *Nat. Mater.* **2007**, *6*, 291–295.
(16) Desvaux, C.; Amiens, C.; Fejes, P.; Renaud, P.; Respaud, M.; Lecante, P.; Snoeck, E.; Chaudret, B. *Nat. Mater.* **2005**, *4*, 750–753.
(17) Sonnichsen, C.; Reinhard, B. M.; Liphardt, J.; Alivisatos, A. P. *Nat. Biotechnol.* **2005**, *23*, 741–745.
(18) Sun, S. H.; Murray, C. B. *J. Appl. Phys.* **1999**, *85*, 4325–4330.
(19) Brown, L. V.; Sobhani, H.; Lassiter, J. B.; Nordlander, P.; Halas, N. J. *ACS Nano* **2010**, *4*, 819–832.
(20) Liu, J. W.; Lu, Y. *J. Am. Chem. Soc.* **2003**, *125*, 6642–6643.
(21) Denisyuk, A. I.; Adamo, G.; MacDonald, K. F.; Edgar, J.; Arnold, M. D.; Myroshnychenko, V.; Ford, M. J.; de Abajo, F. J. G.; Zheludev, N. I. *Nano Lett.* **2010**, *10*, 3250–3252.
(22) Alivisatos, A. P.; Johnsson, K. P.; Peng, X. G.; Wilson, T. E.; Loweth, C. J.; Bruchez, M. P.; Schultz, P. G. *Nature* **1996**, *382*, 609–611.
(23) Chen, C. L.; Zhang, P. J.; Rosi, N. L. *J. Am. Chem. Soc.* **2008**, *130*, 13555–13557.
(24) Mirkin, C. A.; Letsinger, R. L.; Mucic, R. C.; Storhoff, J. J. *Nature* **1996**, *382*, 607–609.
(25) Chen, C. L.; Rosi, N. L. *J. Am. Chem. Soc.* **2010**, *132*, 6902–6903.
(26) Zubarev, E. R.; Xu, J.; Sayyad, A.; Gibson, J. D. *J. Am. Chem. Soc.* **2006**, *128*, 15098–15099.
(27) Caswell, K. K.; Wilson, J. N.; Bunz, U. H. F.; Murphy, C. J. *J. Am. Chem. Soc.* **2003**, *125*, 13914–13915.
(28) (a) Nie, Z. H.; Fava, D.; Kumacheva, E.; Zou, S.; Walker, G. C.; Rubinstein, M. *Nat. Mater.* **2007**, *6*, 609–614. (b) Nie, Z.; Fava, D.; Winnik, M. A.; Rubinstein, M.; Kumacheva, E. *J. Am. Chem. Soc.* **2008**, *130*, 3683–3689. (c) Fava, D.; Nie, Z.; Winnik, M. A.; Kumacheva, E. *Adv. Mater.* **2008**, *20*, 4318–4322.
(29) Joseph, S. T. S.; Ipe, B. I.; Pramod, P.; Thomas, K. G. *J. Phys. Chem. B* **2006**, *110*, 150–157.
(30) Jain, P. K.; Eustis, S.; El-Sayed, M. A. *J. Phys. Chem. B* **2006**, *110*, 18243–18253.
(31) Link, S.; Mohamed, M. B.; El-Sayed, M. A. *J. Phys. Chem. B* **1999**, *103*, 3073–3077.
(32) Slaughter, L. S.; Wu, Y. P.; Willingham, B. A.; Nordlander, P.; Link, S. *ACS Nano* **2010**, *4*, 4657–4666.

(33) Funston, A. M.; Novo, C.; Davis, T. J.; Mulvaney, P. *Nano Lett.* **2009**, *9*, 1651–1658.
(34) Addison, C. J.; Brolo, A. G. *Langmuir* **2006**, *22*, 8696–8702.
(35) Hu, X; Cheng, W; Wang, T; Wang, Y; Wang, E; S, D. *J. Phys. Chem. B* **2005**, *109*, 19385–19389.
(36) Nikoobakht, B.; El-Sayed, M. A. *J. Phys. Chem. A* **2003**, *107*, 3372–3378.
(37) Chen, G.; Wang, Y.; Tan, L. H.; Yang, M. X.; Tan, L. S.; Chen, Y.; Chen, H. Y. *J. Am. Chem. Soc.* **2009**, *131*, 4218–4219.
(38) Goddard, G.; Brown, L. O.; Habbersett, R.; Brady, C. I.; Martin, J. C.; Graves, S. W.; Freyer, J. P.; Doorn, S. K. *J. Am. Chem. Soc.* **2010**, *132*, 6081–6090.
(39) Laurence, T. A.; Braun, G.; Talley, C.; Schwartzberg, A.; Moskovits, M.; Reich, N.; Huser, T. *J. Am. Chem. Soc.* **2009**, *131*, 162–169.
(40) Chen, T.; Wang, H.; Chen, G.; Wang, Y.; Feng, Y. H.; Teo, W. S.; Wu, T.; Chen, H. Y. *ACS Nano* **2010**, *4*, 3087–3094.
(41) Felidj, N.; Aubard, J.; Levi, G.; Krenn, J. R.; Hohenau, A.; Schider, G.; Leitner, A.; Aussenegg, F. R. *Appl. Phys. Lett.* **2003**, *82*, 3095–3097.
(42) Felidj, N.; Aubard, J.; Levi, G.; Krenn, J. R.; Salerno, M.; Schider, G.; Lamprecht, B.; Leitner, A.; Aussenegg, F. R. *Phys. Rev. B* **2002**, *65*, 075419.
(43) Nikoobakht, B.; El-Sayed, M. A. *Chem. Mater.* **2003**, *15*, 1957–1962.
(44) Taflove, A.; Hagness, S. C. *Computational Electrodynamics: The Finite-Difference Time Domain Method*, 2nd ed.; Artech House: Boston, 2000.
(45) Johnson, P. B.; Christy, R. W. *Phys. Rev. B* **1972**, *6*, 4370–4379.
(46) Liu, K.; Nie, Z. H.; Zhao, N. N.; Li, W.; Rubinstein, M.; Kumacheva, E. *Science* **2010**, *329*, 197–200.
(47) Prodan, E.; Nordlander, P. *J. Chem. Phys.* **2004**, *120*, 5444–5454.
(48) Tabor, C.; Van Haute, D.; El-Sayed, M. A. *ACS Nano* **2009**, *3*, 3670–3678.
(49) Shao, L.; Woo, K. C.; Chen, H. J.; Jin, Z.; Wang, J. F.; Lin, H. Q. *ACS Nano* **2010**, *4*, 3053–3062.
(50) Brolo, A. G.; Sanderson, A. C. *Can. J. Chem.* **2004**, *82*, 1474–1480.
(51) Brolo, A. G.; Sanderson, A. C.; Smith, A. P. *Phys. Rev. B* **2004**, *69*, 045424.
(52) Aroca, R. *Surface-enhanced vibrational spectroscopy*; John Wiley & Sons: New York, 2006.
(53) Moskovits, M. *J. Chem. Phys.* **1982**, *77*, 4408–4416.
(54) Moskovits, M.; Suh, J. S. *J. Phys. Chem.* **1984**, *88*, 5526–5530.
(55) Kneipp, K.; Kneipp, H.; Itzkan, I.; Dasari, R. R.; Feld, M. S. *Chem. Rev.* **1999**, *99*, 2957–2975.
(56) Moskovits, M. *Rev. Mod. Phys.* **1985**, *57*, 783–826.
(57) Schatz, G. C.; Young, M. A.; Van Duyne, R. P. In *Surface-Enhanced Raman Scattering: Physics and Applications*, Topics in Applied Physics 103; Kneipp, K., Moskovits, M., Kneipp, H., Eds.; Springer: Berlin, 2006; pp 19−45.
(58) Weitz, D. A.; Garoff, S.; Gersten, J. I.; Nitzan, A. *J. Chem. Phys.* **1983**, *78*, 5324–5338.
(59) Kelly, K. L.; Coronado, E.; Zhao, L. L.; Schatz, G. C. *J. Phys. Chem. B* **2003**, *107*, 668–677.
(60) Le Ru, E. C.; Galrefloway, C.; Etchegoin, P. G. *Phys. Chem. Chem. Phys.* **2006**, *8*, 3083–3087.